Molten pool behaviour and its physical mechanism during selective laser melting of TiC/AlSi10Mg nanocomposites: simulation and experiments

Molten pool behaviour and its physical mechanism during selective laser melting of TiC/AlSi10Mg nanocomposites: simulation and experiments

Pengpeng Yuan[1,2] and Dongdong Gu[1,2]

[1] College of Materials Science and Technology, Nanjing University of Aeronautics and Astronautics, Yudao Street 29, Nanjing 210016, People's Republic of China
[2] Institute of Additive Manufacturing (3D Printing), Nanjing University of Aeronautics and Astronautics, Yudao Street 29, Nanjing 210016, People's Republic of China

E-mail: dongdonggu@nuaa.edu.cn

Abstract

Simulation of temperature evolution and thermal behaviour of the molten pool during selective laser melting (SLM) of TiC/AlSi10Mg nanocomposites was performed, using a finite volume method. Some important physical phenomena, such as a transition from powder to solid, nonlinearities produced by temperature-dependent material properties and fluid flow, were taken into account in the calculation. The effects of Marangoni convection and SLM processing parameters, such as laser power and scan speed, on temperature evolution behaviour, molten pool dimensions and liquid lifetime were thoroughly investigated. The simulation results showed that Marangoni convection played a crucial role in intensifying the convective heat transfer and changing the molten pool geometry. The temperature of laser–powder interaction zone, the molten pool dimensions and liquid lifetime increased with increasing laser power or decreasing scan speed. The maximum temperature gradient within the molten pool increased significantly with increasing the applied laser power, but increased slightly as a higher scan speed was applied. The experimental study on the interlayer bonding and densification behaviour and the surface morphologies and balling effect of the SLM-processed TiC/AlSi10Mg nanocomposites parts was performed. The experimental results validated the thermal behaviour and underlying physical mechanism of the molten pool obtained in the simulations.

Keywords: additive manufacturing, selective laser melting, numerical simulation, temperature evolution, aluminium based nanocomposites

(Some figures may appear in colour only in the online journal)

Nomenclature

A	Laser absorptivity of the powder
C_p	Specific heat capacity at constant pressure ($J\,kg^{-1}\,K^{-1}$)
D_P	Diameter of powder particles (m)
F	Body force, e.g. gravity and buoyancy forces (N)
F_0	View factor, 1/3
h	Sensible enthalpy ($J\,kg^{-1}$)
h_c	Convective heat transfer coefficient ($W\,m^{-2}\,K^{-1}$)
h_{ref}	Reference enthalpy ($J\,kg^{-1}$)
H	Enthalpy of the material ($J\,kg^{-1}$)
ΔH	Latent heat of phase change ($J\,kg^{-1}$)
M_s	Mass source (kg)
p	Pressure (Pa)
P	Laser power (W)
q	Laser heat flux ($W\,m^{-2}$)

Q	Heat quantity (J)
r	Radial distance from a point to the centre of the laser beam (m)
S_H	Source item of the energy conservation equation
t	Time (s)
T	Temperature (K)
T_0	Ambient temperature (K)
T_P	Temperature of powders (K)
T_{ref}	Reference temperature (K)
V	Scan speed (mm s^{-1})
$\overrightarrow{V}$	Overall velocity vector (m s^{-1})
u, v	Velocity magnitude (m s^{-1})
x, y, z	Coordinates (m)
X, Y, Z	Coordinate axis
α_i	Volume fraction of each phase
γ	Surface tension (N m^{-1})
ε	Radiation emissivity
κ	Thermal conductivity of powder bed (W m^{-1} K^{-1})
κ_{eff}	Effective thermal conductivity of powder system (W m^{-1} K^{-1})
κ_g	Thermal conductivity of the ambient gas (W m^{-1} K^{-1})
κ_r	Thermal conductivity due to the radiation among particles (W m^{-1} K^{-1})
κ_s	Thermal conductivity of the solid (W m^{-1} K^{-1})
μ	Dynamic viscosity (Pa s)
ρ	Density (kg m^{-3})
σ_e	Stefan–Boltzmann constant
Φ	Initial porosity of powder bed
ω	Radius of the laser beam (m)

1. Introduction

In recent years, the ceramic particulate reinforced aluminum matrix composites (AMCs) have received substantial attention from the aerospace, automobile, microelectronics, and other industries [1–3]. Nanoscale particle reinforced AlSi10Mg nanocomposites, as the newly emerged advanced engineering materials in modern industries, have shown great potential for applications in these fields due to their light weight, low coefficient of thermal expansion, high specific strength, stiffness and elastic modulus, as well as increased tribological properties at elevated temperatures [4–7]. TiC ceramic exhibits a variety of excellent advantages, such as high elastic modulus, high melting point, high hardness and low heat conductivity, especially its good wettability and thermodynamic stability within the molten aluminum, and accordingly is considered to be an ideal reinforcement for Al-based composites [8, 9]. Nevertheless, because of the high affinity to oxygen of AMCs, the main obstacle to fabricate TiC/AlSi10Mg nanocomposites components through traditional processing methods is oxidation, which is detrimental to the mechanical properties of the final parts. Besides, the increasing requirements for geometrically complex components, which are difficult to be prepared via conventional methods, are driving the researches to produce AMCs parts through novel manufacturing techniques.

Selective laser melting (SLM), as a newly established branch of additive manufacturing (AM), is capable of producing complex shaped metal components direct from powder materials [10–13]. During the SLM process, the three-dimensional part to be fabricated is firstly mathematically sliced into thin layers according to the computer-aided design (CAD) model of the object. Then the object is created by selectively fusing and consolidation of the thin deposited powder layers with a moving Gaussian laser heat source in a layer-by-layer manner [14]. With the protective inert gas fed into the sealed building chamber, the interior oxygen content can be reduced below a required standard. Under this condition, the formation of oxide films on the surfaces of the melt can be alleviated. Therefore, AlSi10Mg alloy parts can be obtained successfully through SLM technique [15–18]. Nevertheless, laser based SLM technique involves a complex non-equilibrium physical and chemical metallurgical process, exhibiting complicated mechanism of heat and mass transfer [19–21]. Furthermore, the laser–powder interaction is so quick that the powder materials undergo solid–liquid–solid transition in a very short time, which results in the large temperature gradient and thermal stress and may cause cracks in the final products. For SLM manufacturing of AMCs, due to the high thermal conductivity of Al, the laser energy input is easily dissipated during heat conduction along the previously fabricated layers and heat transfer within the powder bed. The temperature of the molten pool accordingly decreases, producing the considerably high viscosity and poor flowability of the molten material. Thus it is difficult to effectively wet the base material and may result in balling phenomena and other defects such as internal pores and cracks caused by the limited liquid/solid wettability. The above mentioned imperfections are temperature related. However, because of the short laser–powder interaction time and resultant rapid melting and consolidation of powder material, as well as the extremely small molten pool dimensions of several tens of micrometres to hundreds of micrometres, it is difficult to obtain the transient temperature variation through experiment methods. Therefore, it is important to operate numerical simulation to analyse the temperature evolution behaviour during the SLM process.

Numerical simulation of temperature evolution behaviour in the laser–powder interaction zone is also the basis for feedback of laser processing parameters in manufacturing. Up to now, a number of researchers have put their efforts towards understanding the SLM process and establishing models to describe SLM thermal behaviour. Roberts *et al* [22] established a three-dimensional finite element model for predicting the transient temperature field for multiple layers of laser-produced parts, taking into account the laser energy absorption including the nonlinearities produced by temperature-dependent material properties and phase changes. The results demonstrated that the temperature-dependent thermophysical properties played a crucial role in determining the temperature evolution during laser process. Yadroitsev *et al* [23] numerically calculated and analysed the temperature distribution and the molten pool shape during the SLM process of 316L stainless steel parts. In their study, the effects of

the processing parameters such as scanning speed and laser power on single tracks formation were explored. Zhang *et al* [24] investigated the effects of processing parameters of scan velocity, laser power, scan interval and preheating process on temperature field distribution of W–Ni–Fe powder system during the SLM process through establishing a 3D model based on finite element analysis theory. Mazumder *et al* [25] developed a two-dimensional transient model to analyse the convective heat transfer and fluid flow in a weld pool generated by a stationary band laser source. It was well concluded that Marangoni convection caused by surface tension gradient of the molten material had a significant effect on the molten pool shape and dimensions.

In the present study, a three-dimensional finite volume method (FVM) model was developed using the hydrodynamic software FLUENT to simulate the temperature evolution behaviour and molten pool dynamics during the SLM process. The significant effect of Marangoni convection on heat and mass transfer as well as the melt pool configuration were considered with the comparative study of simulation models with and without Marangoni convection. Besides, the transition from powder to solid, the utilization of moving laser source with a Gaussian distribution and the nonlinearities produced by temperature-dependent material properties were all taken into account in the calculation and, thus, a more accurate model was established. The whole information of the temperature evolution history under different laser processing conditions, the molten pool dynamics and the melt characteristics were thoroughly understood through analysing the numerical results. Meanwhile, the SLM experiments were also conducted under the same laser processing parameters used in the simulations. The potential physical metallurgical mechanisms of these temperature-related defects involved in the SLM process were elucidated in details with the combined study of numerical simulation and experiment validation.

2. Modelling approach and numerical simulation

2.1. Physical description of SLM

When an incident laser beam strikes the surface of a powder bed, most of the concentrated flux of energy is absorbed by the powder particles, leading to localized melting. After the moving Gaussian laser heat source leaves the melt region, which is called the molten pool, rapid consolidation of the molten metal powders occurs. During the SLM process, heat transfer mechanism mainly includes heat radiation to powder layer from laser beam, heat conduction among powder particles, and heat convection between powder bed and ambient atmosphere. The three coupled heat transfer mechanisms make the thermal behaviour during the SLM process become very complex. Considering the complicated physical and chemical metallurgical phenomena between the moving Gaussian laser heat source and powder particles, a schematic diagram of SLM physical model is depicted in figure 1. The silver and black particles in the powder bed are AlSi10Mg and TiC powder particles, respectively.
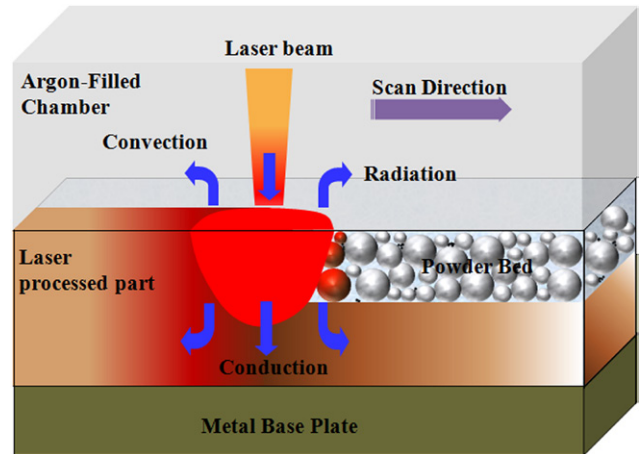

Figure 1. Schematic of the SLM physical model.

2.2. Model development and basic assumptions

The three-dimensional FVM model and laser multi-track scan strategy are depicted in figure 2. The dimensions of the computational model of the TiC/AlSi10Mg powder bed are $3 \times 1 \times 0.08\,\text{mm}^3$. The calculation is carried out with a uniform structured mesh composed of 30 000 hexahedral cells, which are beneficial for obtaining a compromise of computation time and accuracy. Meanwhile, a relatively coarse mesh is adopted for the aluminum substrate. In order to make the complicated problem mathematically tractable, the following assumptions are proposed. During the SLM process, the laser energy can be regarded as the form of heat flow density imported into the power bed from the top of the powder layer, which obeys the Gaussian heat source distribution. The whole powder bed is considered to be the homogeneous and continuous media. Meanwhile, the fluid motion in the molten pool is assumed to be Newtonian, laminar and incompressible and surface of the molten pool is assumed to be flat, neglecting surface rippling [26, 27]. During the melting process, except thermal conductivity, specific heat and surface tension, the other thermal physical parameters of the used materials are assumed to be temperature independent. Due to the unavailability of the surface tension of AlSi10Mg, the surface tension (γ, N m^{-1}) of Al–Si alloy is chosen and listed in table 1. Nevertheless, the coefficient of heat convection between powder bed and surrounding gaseous environment is taken as a constant.

2.3. Governing equations

It is well known that the motion of the fluid generally follow three basic physical conservation laws, namely the conservation of mass, momentum and energy. Based on the above assumptions, the mass, momentum and energy conservation can be expressed in three-dimensional Cartesian coordinate system as follows [29].

Continuity equation:

$$\frac{\partial \rho}{\partial t} + \nabla \cdot (\rho \vec{V}) = M_{\text{s}}. \tag{1}$$
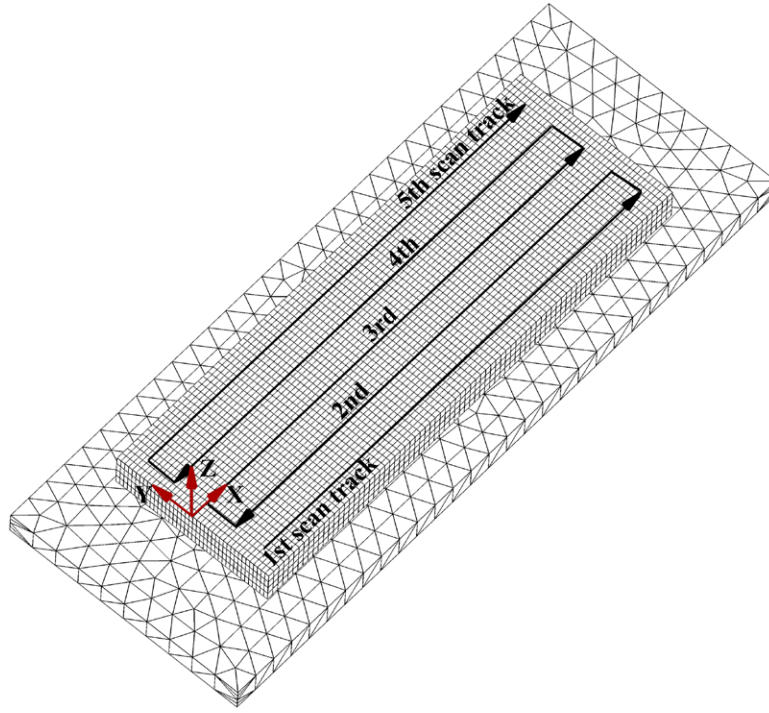
Figure 2. The established three-dimensional FVM model and multi-track scan strategy during the SLM process.

Table 1. The as-used material properties and SLM processing parameters.

Parameter	Value
Laser absorptivity of the AlSi10Mg powder	0.09 [15]
Laser absorptivity of the TiC powder	0.82 [36]
Ambient temperature, T_0	300 K
Surface tension, γ	$(1000.726 - 0.152T) \times 10^{-3}\,\mathrm{N\,m^{-1}}\,T > 873.2\,\mathrm{K}$ [28]
Marangoni coefficient, $\partial\gamma/\partial T$	$-3 \times 10^{-4}\,\mathrm{N\,m^{-1}\,K^{-1}}$ [34]
Powder layer thickness, l_P	$50\,\mu m$
Hatching space, s	$50\,\mu m$
Radius of the laser beam, ω	$35\,\mu m$
Laser power, P	80, 100, 150, 200 W
Scan speed, V	100, 150, 200, 400 mm s^{-1}

Momentum equation:

$$\rho\left(\frac{\partial \overrightarrow{V}}{\partial t} + \overrightarrow{V} \cdot \nabla \overrightarrow{V}\right) = \mu\,\nabla^2\,\overrightarrow{V} - \nabla p + M_s \cdot \overrightarrow{V} + F. \quad (2)$$

Energy equation:

$$\rho\left(\frac{\partial T}{\partial t} + \overrightarrow{V} \cdot \nabla T\right) = \nabla \cdot (\kappa\,\nabla T) + S_H \quad (3)$$

where ρ, κ, μ, p represent density, thermal conductivity, dynamic viscosity and pressure, respectively. $\overrightarrow{V}$ is motion velocity of the melt, M_s is a mass source, F refers to body force (e.g. gravity and buoyancy forces), S_H is the source item of the energy equation and can be defined as

$$S_H = -\rho\left(\frac{\partial}{\partial t}\Delta H + \nabla \cdot (\overrightarrow{V}\Delta H)\right) \quad (4)$$

Where ΔH is the latent heat of phase change.

2.4. Description of moving Gaussian heat source model

According to the first law of thermodynamics, the general energy balance equation in the closed system can be written as

$$Q_L = Q_{CD} + Q_{CV} + Q_R \quad (5)$$

where Q_L, Q_{CD}, Q_{CV} and Q_R represent the input laser energy, conduction, convection losses and radiation losses, respectively. In the present study, the Gaussian heat source model, which is the most widely adopted model, utilizes the symmetrical distribution of laser irradiance across the beam. The mathematic expression of the input heat flux q can be defined as [30]

$$q = \frac{2AP}{\pi\omega^2}\exp\left(-\frac{2r^2}{\omega^2}\right) \quad (6)$$

where A is the laser absorptance of the powder system, P is the laser power, ω represents radius of the Gaussian laser beam, which means the distance from the centre of laser beam to the

J. Phys. D: Appl. Phys. **48** (2015) 035303

P Yuan and D Gu

point where heat flow density mitigates to $1/e^2$ times of that at the centre of laser beam, r is the distance of a point on the surface of the powder bed measured from the laser beam centre at time t and can be expressed as

$$r^2 = (|x| - |V \cdot t|)^2 + |y|^2 \quad (7)$$

where $|x|$ and $|y|$ represent the distance along X- and Y-axis, respectively, and V means the laser scan speed.

The absorptance of metal powders is known to vary between the in-coupling absorptance as proposed by Kruth *et al* [31] to a few per cent when the metal melts. In this study, the laser absorption of powder system is determined by both the physical property of AlSi10Mg and TiC powders and the volume fraction of each phase and can be calculated as

$$A = \sum \alpha_i A_i \quad (8)$$

where α_i stands for the volume fraction of one phase and $\sum_{i-1}^{n} \alpha_i = 1$, n represents the phase number, A_i is the laser absorption of the i phase.

2.5. Treatments of the initial and boundary conditions

The thermal problem to be solved involves a progressive laser beam travelling along the pre-defined path on the surface of the powder bed at a constant velocity. Proper initial and boundary conditions must be set to obtain the more accurate simulation results. Before SLM process starts, the initial condition of the uniform temperature distribution throughout the powder bed at time $t = 0$ can be applied as

$$T(x, y, z, 0) = T_0. \quad (9)$$

T_0 is the ambient temperature taken as $300\,\mathrm{K}$.

On the boundary, the top surface of the powder bed is subject to radiation and convection and imposed heat fluxes. Therefore, the natural boundary condition can be expressed as [32]

$$-\kappa_{\mathrm{eff}} \left(\frac{\partial T}{\partial z} \right)_{z=0} = q - h_{\mathrm{c}}(T - T_0) - \sigma_{\mathrm{e}} \varepsilon \left(T^4 - T_0^4 \right) \quad (10)$$

where κ_{eff} refers to the effective thermal conduction of the powder system, T is temperature, h_{c} is the heat transfer coefficient of natural thermal convection, σ_{e} is the Stefan–Boltzmann constant of $5.67 \times 10^{-8}\,\mathrm{W\,m^{-2}\,K^{-4}}$ and ε is the emissivity.

In the present study, in order to investigate the influence of Marangoni effect, which is caused by the temperature gradient, on heat and mass transfer as well as the resultant melt pool configuration, two comparative simulation models with and without taking into account of the Marangoni effect are established. The major difference of the two cases is the consideration of the surface tension gradient of the molten material on the top surface of the melt pool. The surface tension gradient $(\partial\gamma / \partial T, \mathrm{N\,m^{-1}\,K^{-1}})$ of case 1 (with Marangoni effect), which is also called the Marangoni coefficient, is given by [33]

$$-\mu \frac{\partial u}{\partial z} = \frac{\partial\gamma}{\partial T} \frac{\partial T}{\partial x}, \qquad -\mu \frac{\partial v}{\partial z} = \frac{\partial\gamma}{\partial T} \frac{\partial T}{\partial y}. \quad (11)$$

While in case 2 (without Marangoni effect), the fluid flow is mainly dominated by buoyancy, therefore, the Marangoni coefficient is set as $\partial\gamma / \partial T = 0$. Where u and v are the velocity magnitudes of the fluid in the X and Y directions, respectively.

As regard to the other four lateral surfaces of the powder bed, the coupled heat conduction and convection mechanism suit the boundary conditions well. With the purpose of improving the quality of the manufactured parts, the metal plate needs to preheat to the ambient temperature T_0 before the SLM process starts. Moreover, the bottom of the powder bed adjacent to the metal plate is assumed to be conductive.

2.6. Determination of thermal physical property

During the SLM process, the metal powders AlSi10Mg undergo solid–liquid–solid transition, so the nonlinear behaviour of thermal conductivity and specific heat due to temperature change and phase transformation must be taken into consideration. However, the maximum temperature during the whole process did not exceed the melting point of ceramic powders TiC, therefore, the melting process of TiC particles barely occurs. The variation trend of thermal physical parameters κ and C_p of AlSi10Mg and TiC is shown in figure 3 [35, 36].

Among these thermal physical parameters, the effective thermal conductivity of a loose powder bed is an important material property determining the results of SLM. The comparison of the experimental data with the model of discrete thermal resistances [37, 38] indicates that the effective thermal conductivity of powder bed is proportional to the thermal conductivity of gas filling pores and also depends on the solid fraction and the particle size. For powders with particle size about several tens of micrometres, the effective thermal conductivity is of the order of five to ten times the conductivity of air. Due to the large difference between the thermal conductivity of metals and air, the effective conductivity is mainly determined by the relative density of the powder bed and less by the properties of the powder material, accordingly, the general value can be calculated as [20]

$$\frac{\kappa_{\mathrm{eff}}}{\kappa_{\mathrm{g}}} = (1 - \sqrt{1 - \Phi}) \left(1 + \frac{\Phi \kappa_{\mathrm{r}}}{\kappa_{\mathrm{g}}} \right)$$
$$+ \sqrt{1 - \Phi} \left\{ \frac{2}{1 - \frac{\kappa_{\mathrm{g}}}{\kappa_{\mathrm{s}}}} \left[\frac{1}{1 - \frac{\kappa_{\mathrm{g}}}{\kappa_{\mathrm{s}}}} \ln\left(\frac{\kappa_{\mathrm{g}}}{\kappa_{\mathrm{s}}} \right) - 1 \right] + \frac{\kappa_{\mathrm{r}}}{\kappa_{\mathrm{g}}} \right\} \quad (12)$$

where Φ is the initial porosity of the powder bed, κ_{g} is the thermal conductivity of the ambient gas in the building chamber, κ_{s} is thermal conductivity of the solid, κ_{r} is the thermal conductivity in the powder bed due to radiation among particles and can be further defined as:

$$\kappa_{\mathrm{r}} = 4F_0 \sigma_{\mathrm{e}} T_{\mathrm{P}}^3 D_{\mathrm{P}} \quad (13)$$

where T_{P} is the temperature of the powder particles, D_{P} represents the average particle diameter, F_0 is a view factor which is approximately taken as 1/3.
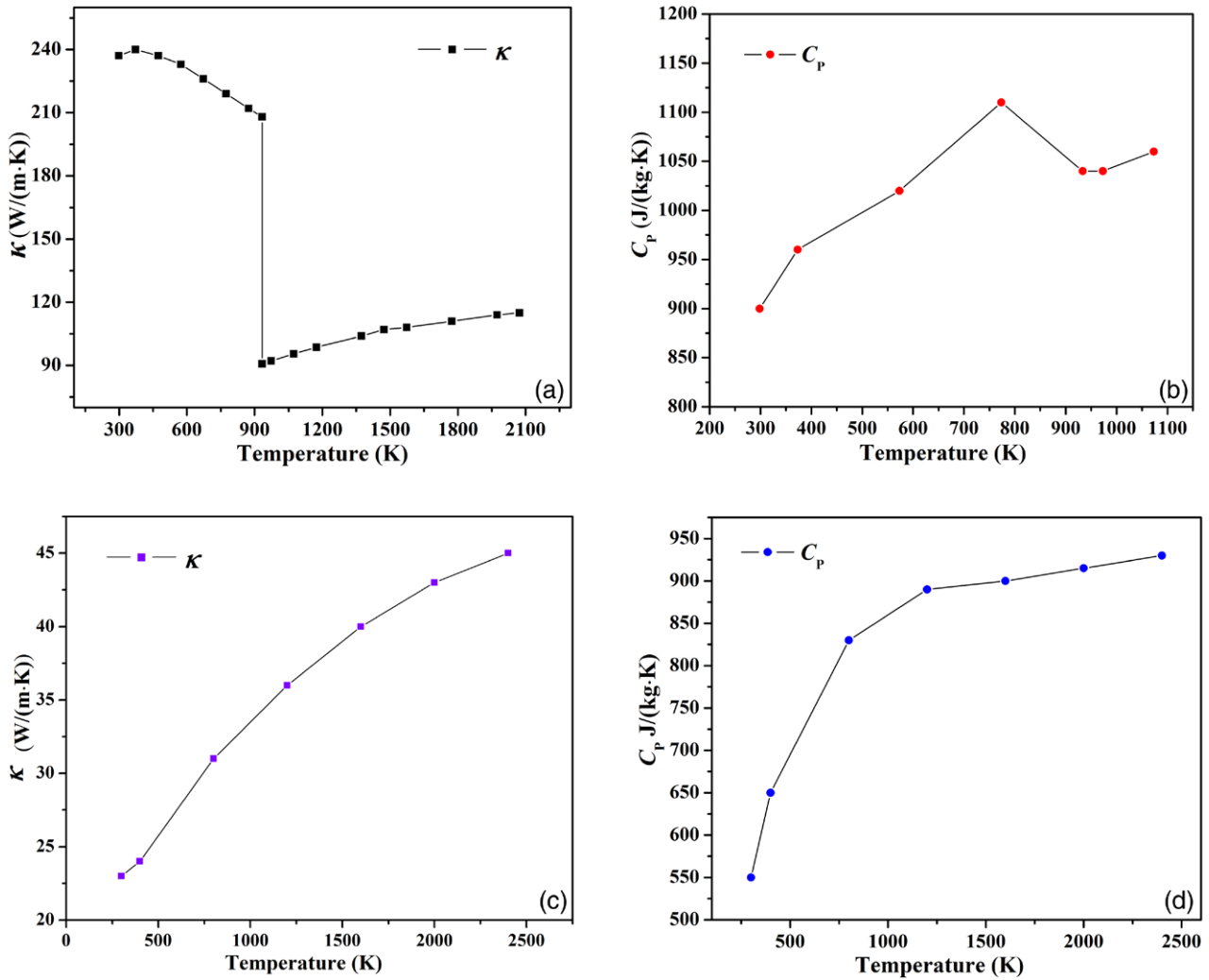
Figure 3. Thermal physical properties of as-used materials: (*a*) thermal conductivity of AlSi10Mg; (*b*) specific heat at a constant pressure of AlSi10Mg; (*c*) and (*d*) are the thermal conductivity and specific heat at a constant pressure of TiC, respectively.

Melting and solidification of a bed of powder particles subjected to temporal Gaussian heat flux from a laser beam must be considered in this model. Moreover, when the material temperature crosses the phase transformation range, the material can absorb or release a large amount of latent heat, which is not negligible during the entire process. To simulate the latent heat of phase change, the enthalpy can be calculated by

$$H = h + \Delta H \tag{14}$$

where H is the enthalpy, h is the sensible enthalpy and $h = h_{\text{ref}} + \int_{T_{\text{ref}}}^{T} C_p \, \mathrm{d}T$, h_{ref} is the reference enthalpy and C_p is the specific heat capacity at constant pressure.

2.7. Numerical method

The numerical simulation is carried out using the computational fluid dynamics software FLUENT 6.3.26 to obtain a thorough understanding of the temperature evolution behaviour during the SLM process. The software is composed of the preprocessor GAMBIT 2.4.6, the solver and the post-processor. GAMBIT 2.4.6 is applied to design the geometry of the model, the mesh and the boundary types of a 3D computational domain. With appropriate boundary conditions, the mass, momentum and energy conservation equations are discretized using control volume method and then solved adopting Semi-Implicit Method for Pressure Linked Equation Consistent (SIMPLEC) algorithm. Typically, the time step is restricted to be no more than 10^{-5} s to satisfy the convergence criteria requested by the governing equations, as well as the movement of the liquid/gas interface. The as-used material properties and SLM processing parameters are shown in table 1.

3. Experimental procedures

The starting powder system consisted of two components, i.e. the 99.0% purity TiC nanopowder with a near spherical shape and a mean particle size of 50 nm and the 99.7% purity AlSi10Mg powder with a spherical shape and an average particle diameter of 30 μm. The TiC and AlSi10Mg powder

J. Phys. D: Appl. Phys. **48** (2015) 035303

P Yuan and D Gu

components consisting of 5 wt% TiC were mechanically mixed in a Pulverisette 4 vario-planetary mill (Fritsch GmbH, Germany), using a ball-to-powder weight ratio of 1 : 1, a rotation speed of main disc of 200 rpm, and a mixing duration of 4 h. The used SLM system was self-developed and consisted mainly of an IPG YLR-200-SM ytterbium fibre laser with a power of ~200 W and a spot size of 70 μm, an automatic powder spreading device, an inert argon gas protection system, and a computer system for process control. Details concerning SLM processing procedures have been addressed in [10, 11]. Specimens for metallographic examinations were cut, ground and polished according to the standard procedures, and then etched with a solution consisting of 2 ml HF, 3 ml HCl, 5 ml HNO$_3$ and 190 ml distilled water for 10 s. An Olympus PMG3 optical microscope (OM) was used to observe the interlayer microstructures of the SLM-processed specimens. High-resolution study of the surface morphologies of the SLM-processed parts was performed using a Hitachi S-4800 field emission scanning electron microscope (FE-SEM).

4. Results and discussion

4.1. Effect of Marangoni convection on heat and mass transfer

Figure 4 shows the three different sectional views of temperature contour plots of the powder bed during the SLM process with and without Marangoni effect. These two groups of simulation results were obtained under the same laser processing conditions ($P = 150$ W, $V = 400$ mm s^{-1}). The temperature contour plots from top view were observed somewhat stretched to a comet-shaped tail along the laser scanning direction and the temperature distribution was symmetrical in X–Y and Y–Z sections. The arising of this ellipse shape instead of circular shape can be ascribed to the effect of the moving heat source. Moreover, because the isotherms near the front side of the moving laser beam were more closely spaced compared with those in the rear side, the temperature gradient was accordingly larger in melt pool front.

On the other hand, the molten pool dimensions can be measured according to the melting line ($T_m = 873.2$ K) of the AlSi10Mg powder material. In case 1 (with Marangoni effect), the three dimensions of the molten pool were 167.3 μm in length, 124.6 μm in width and 59.2 μm in depth (figures 4(a), (c) and (e)). However, in case 2 (without Marangoni effect), the melt pool was generated with a shorter length of 136.2 μm and a narrower width of 110.4 μm, but with a deeper depth of 70.6 μm (figures 4(b), (d) and (f)). Due to the introduction of the Gaussian distribution laser heat source, large temperature gradients are formed within the laser-induced melt pool. The temperature gradient will lead to a surface tension gradient, which causes a Marangoni flow pointed from low surface tension to high surface tension area on the surface of the melt pool [39]. With the protection of inert gas during the SLM process, since the surface tension is generally a decreasing function of temperature i.e.$\partial \gamma / \partial T < 0$, the higher surface tension of the cooler liquid near the edge of the molten pool tends to pull the liquid away from the centre of the molten pool.

Therefore, the Marangoni flow on the surface of the liquid pool exhibits a radially outward flow pattern (figure 5(a)), thus transferring heat and mass and changing the molten pool geometry [40]. Meanwhile, the flow is upwards in the centre of the molten pool due to the combined effects of gravity and buoyancy forces, which is further impeditive of the heat transfer downwards (figures 5(b) and (c)). With the presence of Marangoni effect, the heat and mass transfer are mainly dominated by Marangoni convection. Accordingly, the melt pool is in a shallow and wide shape. However, the heat conduction becomes the main mechanism of heat transfer in case 2. For a given laser energy input, less heat is transferred from the pool centre to the periphery without Marangoni effect and accordingly, the molten pool turns into a narrower but deeper configuration.

Furthermore, the maximum temperature recorded in case 1 was 1560 K, which was lower than the value of 1590 K in case 2. This phenomenon further proved that the Marangoni effect is beneficial for accelerating the heat and mass transfer within the melt pool by driving the liquid flow. It was noted that the molten material at the free surface flowed from the central outwards to the solid–liquid interface and formed two symmetric vortexes in the melt pool (figure 5(c)). Because the melting point of TiC reinforcement (~3410 K) is lower than the peak operating temperature during SLM process, the solid particles are believed to recirculate a great many times by the carriage of the recirculation of fluid in the molten pool before the melt finally solidifies. The intensity of the fluid flow will significantly affect the dispersion state of the TiC reinforcement within the Al matrix. Meanwhile, there also exists the impediment effect of TiC particles exerted on the fluid flow, which accordingly affects the heat and mass transfer, as well as the resultant molten pool configuration.

4.2. Effect of laser processing conditions on thermal behaviour

Figure 6(a) illustrates the temperature distribution profiles of the powder bed surface along X-axis at $Y = 0$ under the irradiation of laser beam at the third laser scan track. It was observed that the maximum temperatures increased from 1260 to 1720 K with the increase of the laser power from 80 to 200 W (fixed $V = 400$ mm s^{-1}). The curve slopes of the temperature distribution profiles which represent the temperature gradients were found to be varied with the laser power. The maximum temperature gradient (~21.4 K μm^{-1}) during the SLM process at $P_1 = 200$ W was more than twice of that at $P_4 = 80$ W (~9.8 K μm^{-1}). It was well demonstrated the significance of the laser power during the SLM fabrication process. Meanwhile, it was worth noting that the above mentioned temperature gradients referred to those in the front side of the molten pool. However, the maximum thermal gradients emerged in the back side of the liquid pool ranged from 9.1 to 19.8 K μm^{-1}. The quantitative analysis further proved that the temperature gradients in front of the molten pool were larger than those in the back side. According to the four curves as shown in figure 6(b), it was obvious that the molten pool
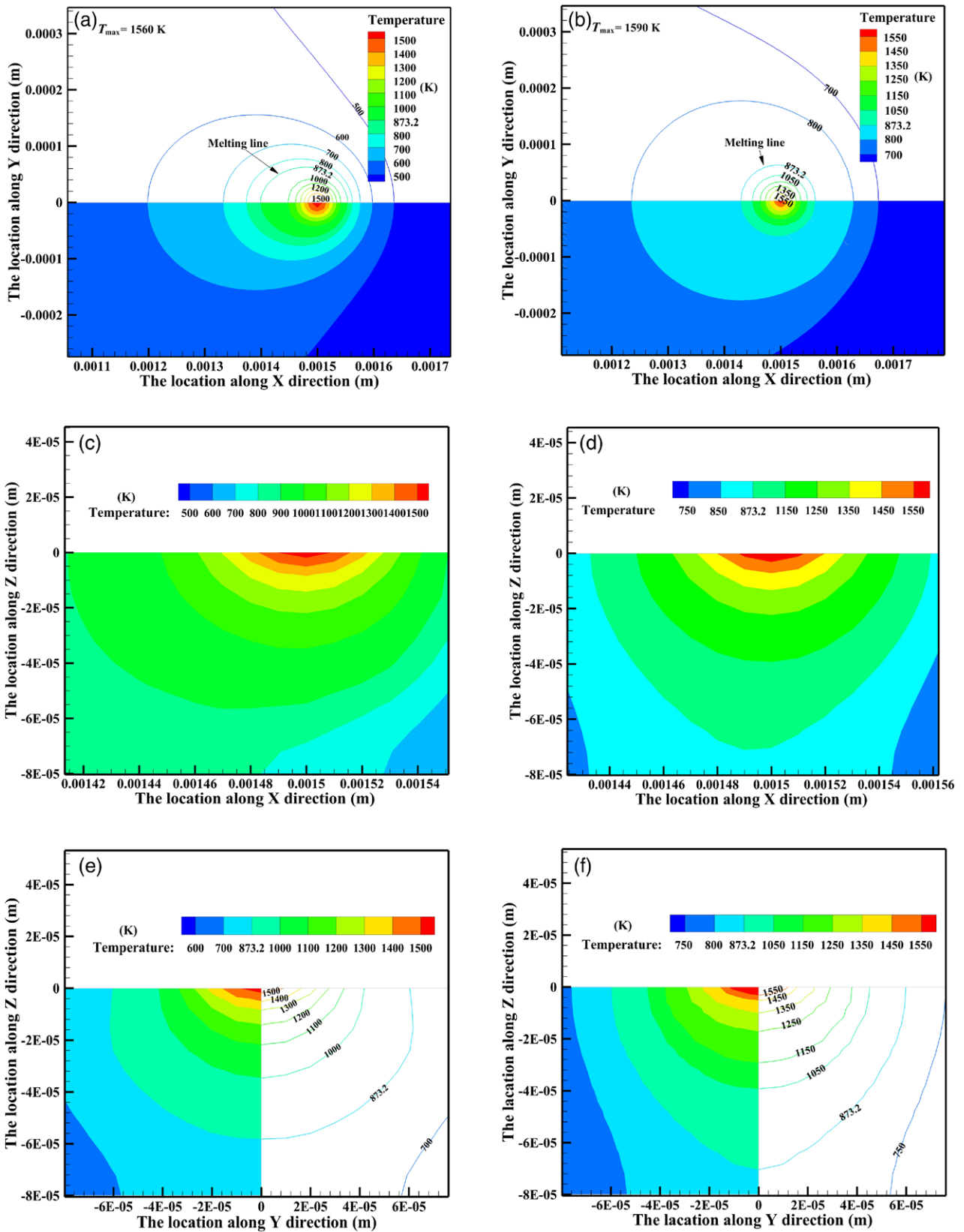
Figure 4. Comparison of temperature contour plots in different views in two different cases. Case 1—with negative Marangoni effect: (*a*) top view; (*c*) longitudinal view at $Y = 0$; (*e*) cross-sectional view at $X = 1.5$ mm; case 2—without Marangoni effect: (*b*) top view; (*d*) longitudinal view at $Y = 0$; (*f*) cross-sectional view at $X = 1.5$ mm (laser power 150 W, scan speed 400 mm s^{-1}, hatching space 50 μm, laser spot size 70 μm, scan track 3).
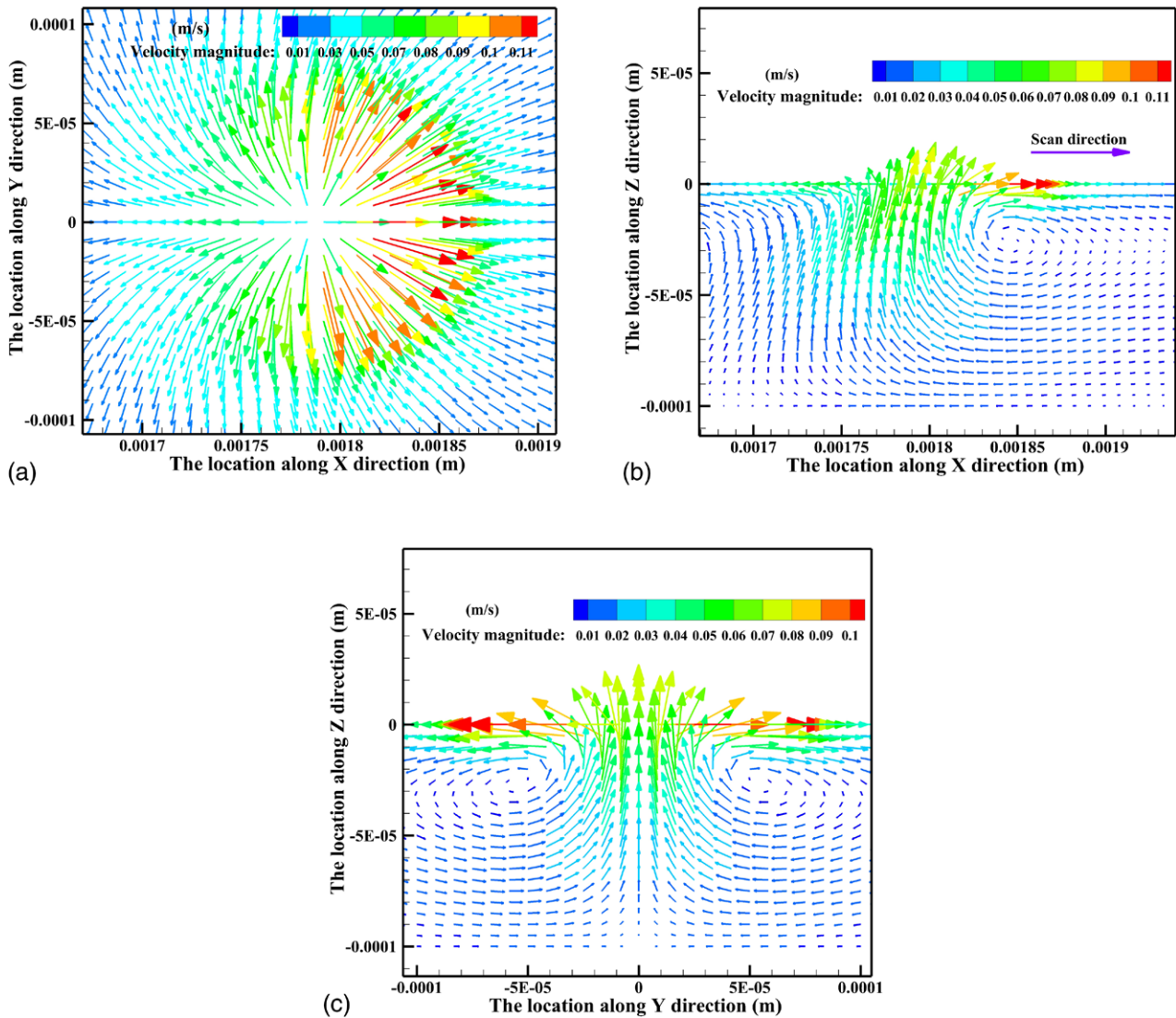
Figure 5. Velocity vector plots in the molten pool with the action of Marangoni effect in different views: (*a*) top view; (*b*) longitudinal view at $Y = 0$; (*c*) cross-sectional view at $X = 1.5$ mm (laser power 150 W, scan speed 400 mm s^{-1}, hatching space 50 μm, laser spot size 70 μm, scan track 3).

was symmetrical about *X*-axis. This can be explained by the fact that within the laser irradiation region, the laser energy density distribution is symmetric about *X*-axis, whereas the region outside the laser-induced pool is still powder phase. Therefore, the thermal conductivity of the same distance from the laser beam centre for the whole *Y*-axis is almost the same. Furthermore, the calculated maximum thermal gradients along *Y*-axis varied from 11.2 to 24.0 K μm^{-1}, which were large than those along *X*-axis if the laser processing conditions were same.

Figure 6(*c*) demonstrates the temperature evolution in depth direction at $X = 1.5$ mm, $Y = 0$. It was clear that the temperature decreased along the powder bed thickness direction, but the rate of decrease depends on the laser power. In addition, the temperature gradient near the top surface of the melt pool was 41.9 K μm^{-1} and decreased to 0.6 K μm^{-1} at the bottom ($P = 200$ W, $V = 400$ mm s^{-1}). Therefore, it was concluded that the temperature gradient was the largest near the top surface of the powder layer. The absorbed laser energy is

easily dissipated to the previously fabricated layer due to the extremely high thermal conductivity (~240 W m^{-1} K^{-1}) of the solid aluminum alloy. Consequently, a low temperature gradient will be induced at the bottom of each layer.

Figure 7 provides the temperature evolution profiles along different paths of the powder bed at different laser scan speeds but with a fixed laser power of 100 W. It was noted that the peak temperature decreased from 1590 to 1390 K with the increase of scan speeds from 100 to 400 mm s^{-1}. This is because when the travelling speed of laser beam increases, the interaction time between powder particles and laser beam decreases and thus results in a lower peak temperature. Furthermore, the curves in figure 7 were observed smoother than those in figure 6, indicating smaller temperature gradients during the SLM process. When the laser scan speed increased from 100 to 400 mm s^{-1}, the maximum temperature gradient along *X*-axis increased from 10.9 to 12.7 K μm^{-1} (figure 7(*a*)), and it enhanced from 13.7 to 15.6 K μm^{-1} along *Y*-axis (figure 7(*b*)). It was interesting to find that the maximum thermal gradient only increased by 14.2% and
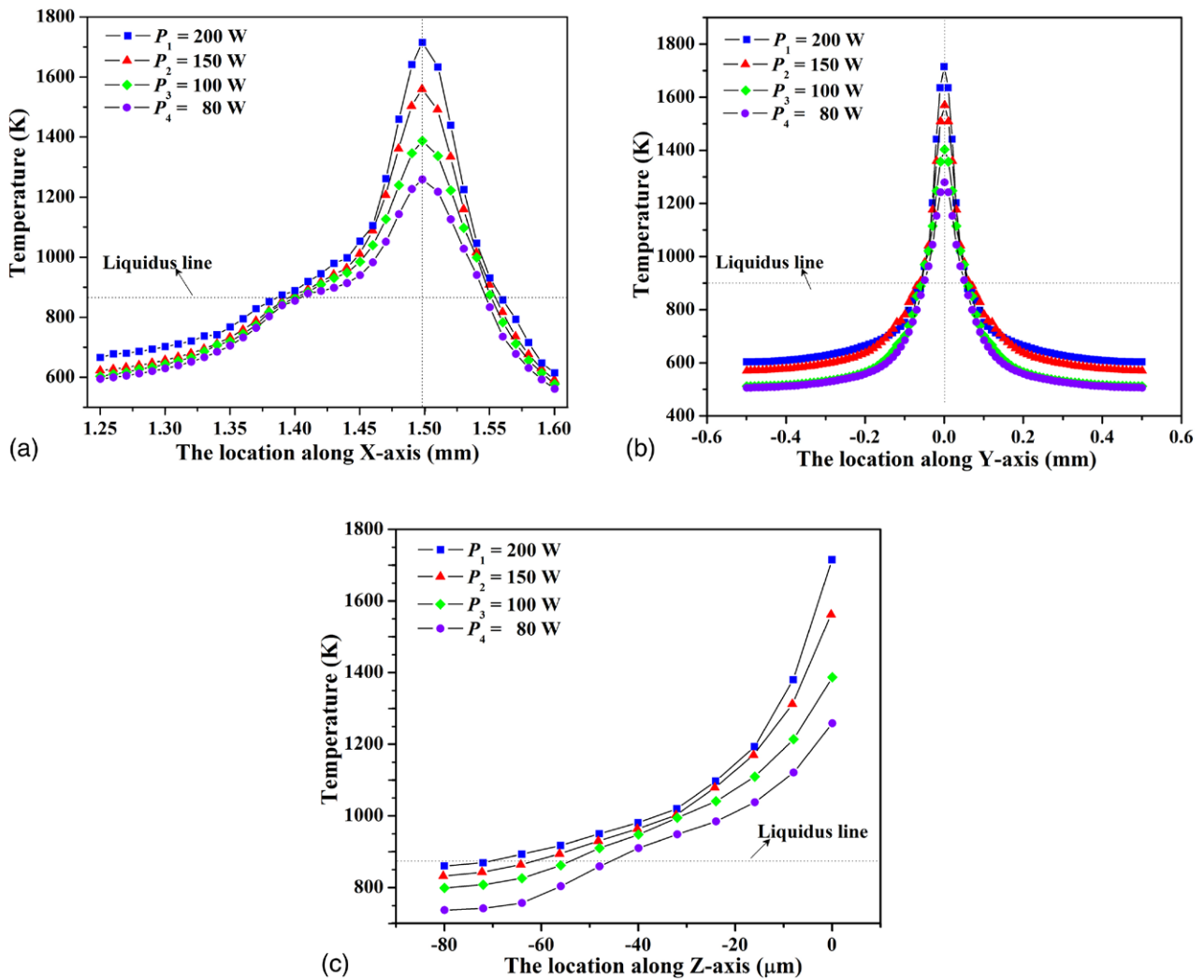
Figure 6. Temperature distribution profiles of powder bed with the action of Marangoni effect at different laser powers with a fixed scan speed of $400 \, \text{mm} \, \text{s}^{-1}$, mapping along different paths: (*a*) *X*-axis at $Y = 0$, $Z = 0$; (*b*) *Y*-axis at $X = 1.5 \, \text{mm}$, $Z = 0$; (*c*) *Z*-axis at $X = 1.5 \, \text{mm}$, $Y = 0$.

12.2% respectively along *X*-axis and *Y*-axis while the laser scan speed became four times of the previous one. Through the quantitative analysis, it was obvious that the effect of laser speed on temperature evolution was much smaller than that of laser power.

4.3. Molten pool dimensions at different SLM processing parameters

Figure 8 depicts the simulated and experimentally measured molten pool dimensions at different processing parameters. The calculation of molten pool sizes was achieved through the above mentioned temperature distribution plots. The region above the liquidus line represented the molten zone, and the distance of the molten material along *X*-axis and parallel to the scan direction was taken as the molten pool length. Similarly, the melt pool width and depth could be obtained. The finally presented melt pool dimensions of experimentation are the average values of experimentally obtained molten pool dimensions by observing the molten pool contours after solidification in both cross-section and longitudinal section of SLM-processed samples.

As illustrated in figure 8(*a*), the molten pool length, width and depth were all found to increase with the increase of the laser power. The calculated length of the molten pool varied from $138.7 \, \mu\text{m}$ at 80 W to $201.2 \, \mu\text{m}$ at 200 W, while the width ranged from 102.8 to $147.3 \, \mu\text{m}$. This phenomenon can be ascribed to the fact that the increase of the laser power results in higher working temperature during SLM process and thus enlarging the melt pool. Meanwhile, the difference between molten pool length and width became more pronounced with the increase of laser power, demonstrating the significance of thermal accumulation effect for high laser power [41]. With respect to molten pool depth, it was only $46.1 \, \mu\text{m}$ ($P_4 = 80 \, \text{W}$), which was less than the power layer thickness and thus detrimental to the completely melting of the whole powder layer. When increasing laser power to 150 and 200 W, the simulated depth could reach 62.8 and $73.2 \, \mu\text{m}$, therefore, good metallurgical bonding with the previously fabricated layer could be obtained. Figure 8(*b*) exhibits the variation of molten pool dimensions with different laser scan speeds while the laser power was fixed at 150 W. It was noted that the molten
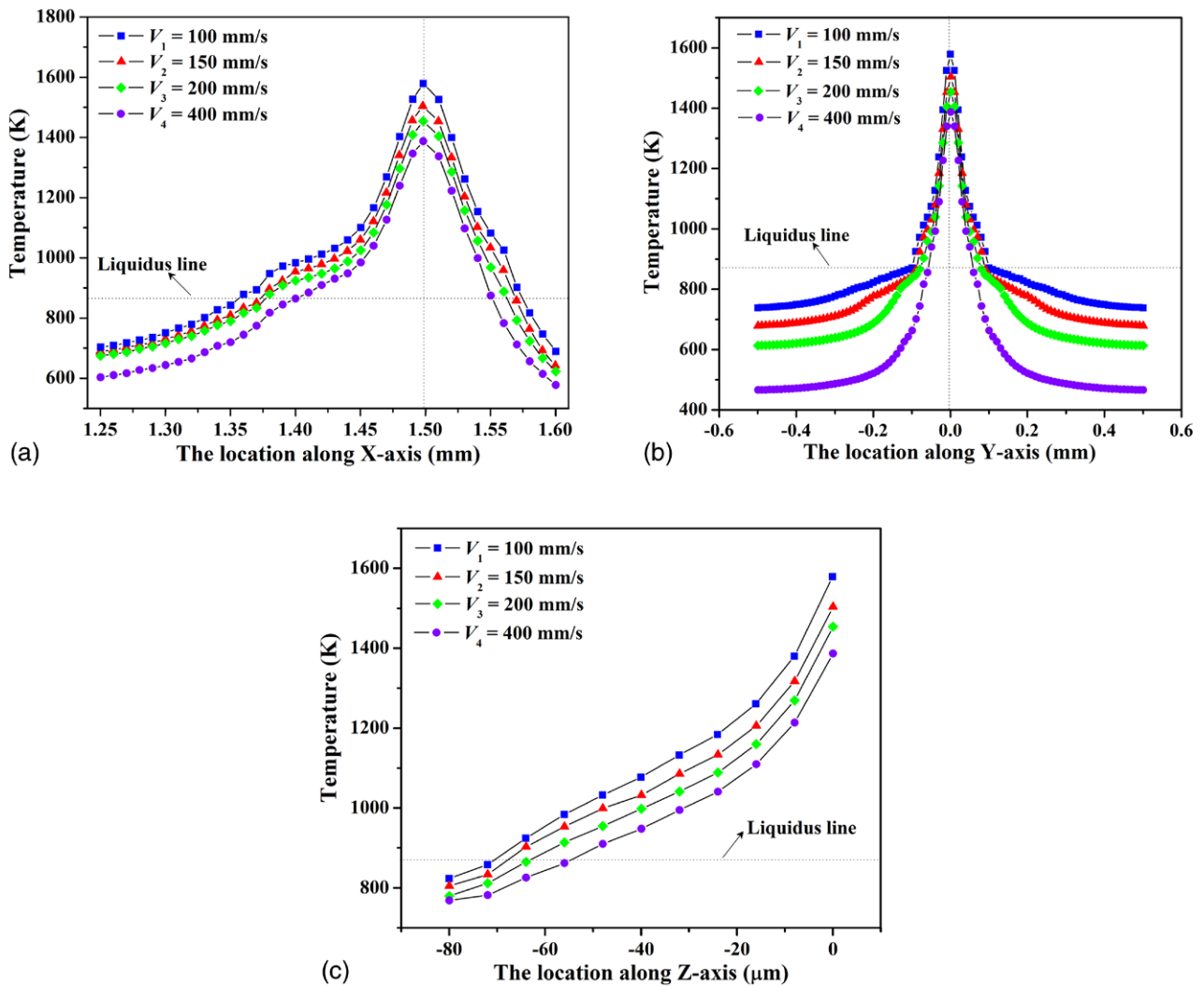
Figure 7. Temperature distribution profiles of the powder bed with the action of Marangoni effect at different scan speeds with a fixed laser power of 100 W, mapping along different paths: (*a*) X-axis at $Y = 0$, $Z = 0$; (*b*) Y-axis at $X = 1.5$ mm, $Z = 0$; (*c*) Z-axis at $X = 1.5$ mm, $Y = 0$.

pool dimensions decreased with the increase of laser scan speed. This is because when the applied laser scan speed is relatively low, the laser–powder interaction time is sufficient long to let the powder material absorb more energy, thereby enlarging the molten region. Meanwhile, the difference between molten pool length and width also increases with the enhancement of scan speed. Furthermore, the simulated molten pool width (e.g. 179.6 μm at $V_2 = 150$ mm s^{-1} and 164.7 μm at $V_3 = 200$ mm s^{-1}) was obviously larger than the hatching space of 50 μm, yielding favourable bonding between neighbouring tracks. The melt pool shapes of simulation predicted and experimentally obtained were observed similar, but still existing somewhat difference in width and depth (figure 8(*c*)), which further validates the accuracy of the simulation models.

4.4. Lifetime of molten pool

Due to the extremely short interaction time between laser beam and the powder particles, the SLM process involves highly non-equilibrium physical and chemical metallurgical phenomena, including rapid melting and solidification process and liquid–solid phase transformation [42]. The duration time from the powder particles in the local region start to melt to the eventually solidification process, which is called liquid lifetime, is introduced to study the molten pool dynamics. The temperature evolution with time at the centre point of the third track for different laser processing conditions is presented in figure 9. It was noted that both the peak temperature and the lifetime of molten pool were observed to enhance as elevated laser power was applied, but decreased with the increase of scan speed. For example, with a fixed scan speed of 400 mm s^{-1}, the liquid lifetime was calculated as 0.34 ms at $P_4 = 80$ W, while it increased to 1.75 ms at $P_1 = 200$ W. This is because increasing the laser power or decreasing the scan speed will enhance the absorbed laser energy, leading to high working temperature and sufficient liquid to wet the surrounding powder particles. A sound wettability was beneficial to lower the melt viscosity and further favoured the spreading of liquid material on the substrate or
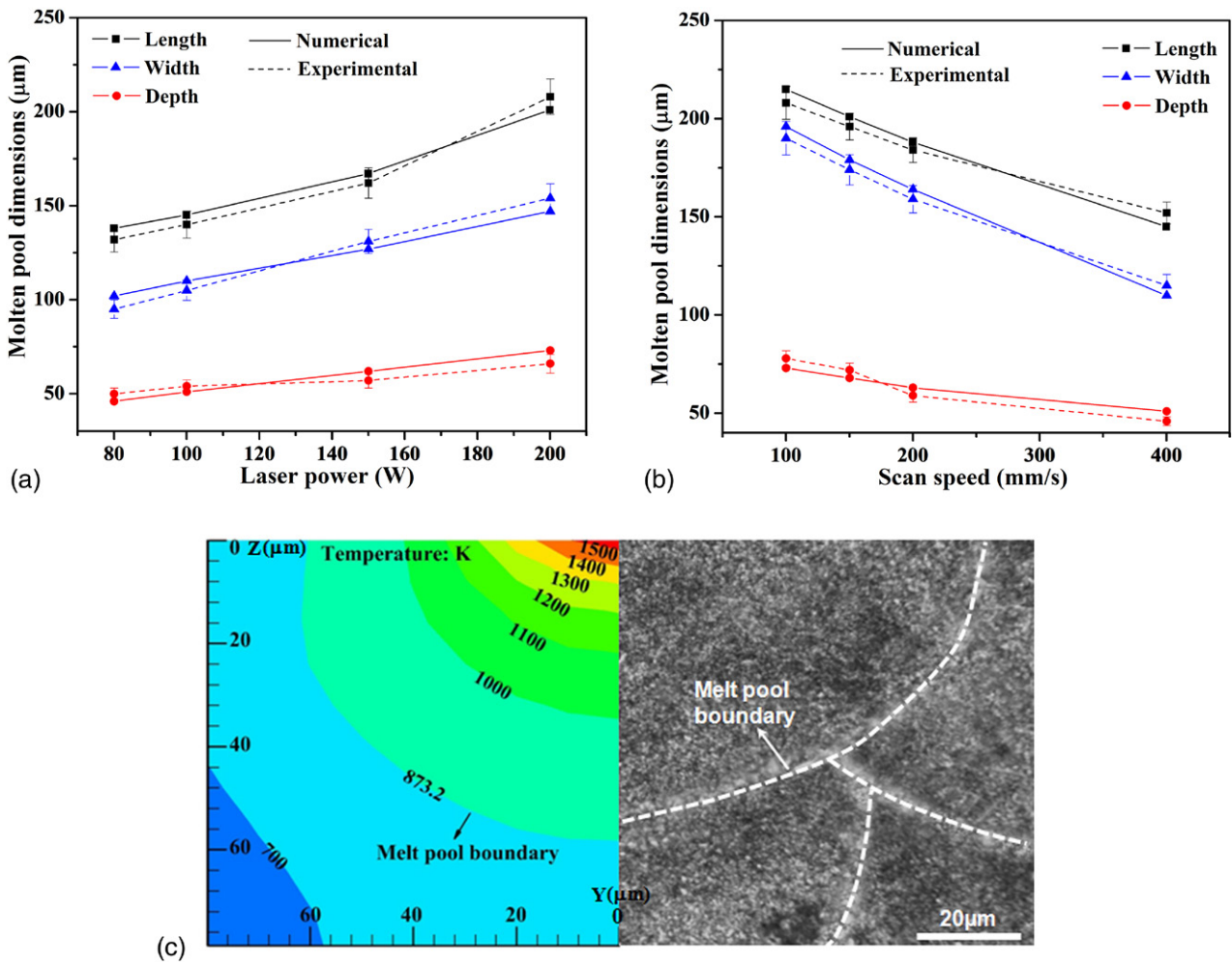
J. Phys. D: Appl. Phys. 48 (2015) 035303

P Yuan and D Gu

Figure 8. The calculated and experimentally measured molten pool dimensions versus laser processing parameters: (*a*) different laser powers with a fixed laser scan speed of 400 mm s^{-1}; (*b*) various laser scan speeds with a fixed laser power of 100 W; (*c*) comparison of simulated (left) and experimental (right) molten pool profiles on cross-section at the same parameters of $P = 150$ W and $V = 400$ mm s^{-1}. The cross-sectional configurations of the tracks are highlighted by the dashed lines.

prefabricated layers, therefore alleviating the occurrence of balling phenomenon and interior porosity [43]. Nevertheless, when the laser beam travelled along the defined tracks at the speed of 100 mm s^{-1}, the lifetime of the melt pool reached 7.41 ms, which may produce too much liquid and form a large molten pool that was difficult to control, therefore a proper care should be paid to choose appropriate laser processing parameters. Furthermore, the simulated cooling rate can reach to 10^6 K s^{-1}, sufficiently exhibiting rapid solidification nature of the SLM process, and it was favourable to obtain fine microstructures and attendant good mechanical properties of the final parts [10].

4.5. Experimental investigations of SLM-processed parts

Figure 10 illustrates the cross-sectional microstructures of SLM-processed TiC/AlSi10Mg nanocomposite components using different laser powers and the constant laser scan speed of 400 mm s^{-1}. Because of the layer-by-layer incremental deposition manner, the layerwise microstructural features were obviously observed in these OM images. Furthermore, it was obvious that the formation of imperfections in SLM-processed

samples, e.g. interior porosity, thermal stresses and attendant microcracks, was significantly influenced by the applied SLM processing conditions. At a relatively high laser power of 200 W, the interlayer microcracks were present in the SLM-produced microstructures (figure 10(*a*)). As illustrated in figure 10(*b*), the dense and coherent metallurgically bonded layers without any apparent pores and cracks were generated as the laser power decreased to 150 W. However, a large number of small micropores with an average size of ~40 μm were detected when a lower laser power of 100 W was applied (figure 10(*c*)). At an even lower laser power of 80 W, it was noted that the residual pores became larger in their sizes, with an average size of ~200 μm. Meanwhile, the pores were present in almost the same positions along several adjacent layers (figure 10(*d*)).

During the SLM process, the metal powder particles experienced rapid melting and consolidation, yielding large temperature gradients and thus accumulating considerable residual stresses in the final parts. At a high laser power of 200 W and attendant large temperature gradient of 4.19 × 10^7 K m^{-1} in Z-direction, microcracks were observed in the interlayer region on the cross-section of SLM-fabricated sample (figure 10(*a*))
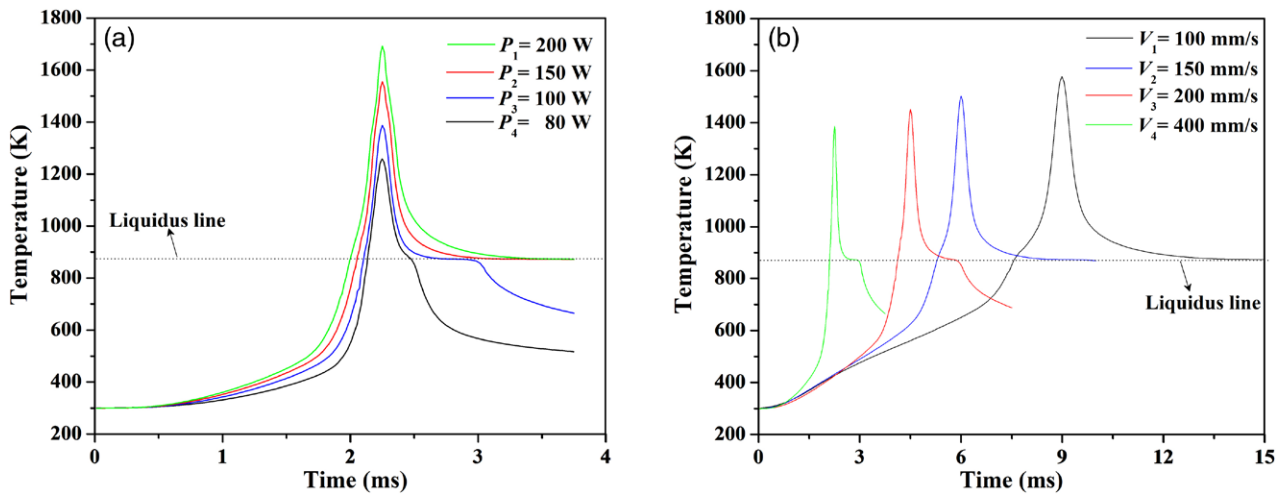
Figure 9. Variations of temperature with time at the centre point of the third track: (*a*) for different laser powers with a fixed scan speed of 400 mm s^{-1}; (*b*) for different scan speeds with a fixed laser power of 100 W.
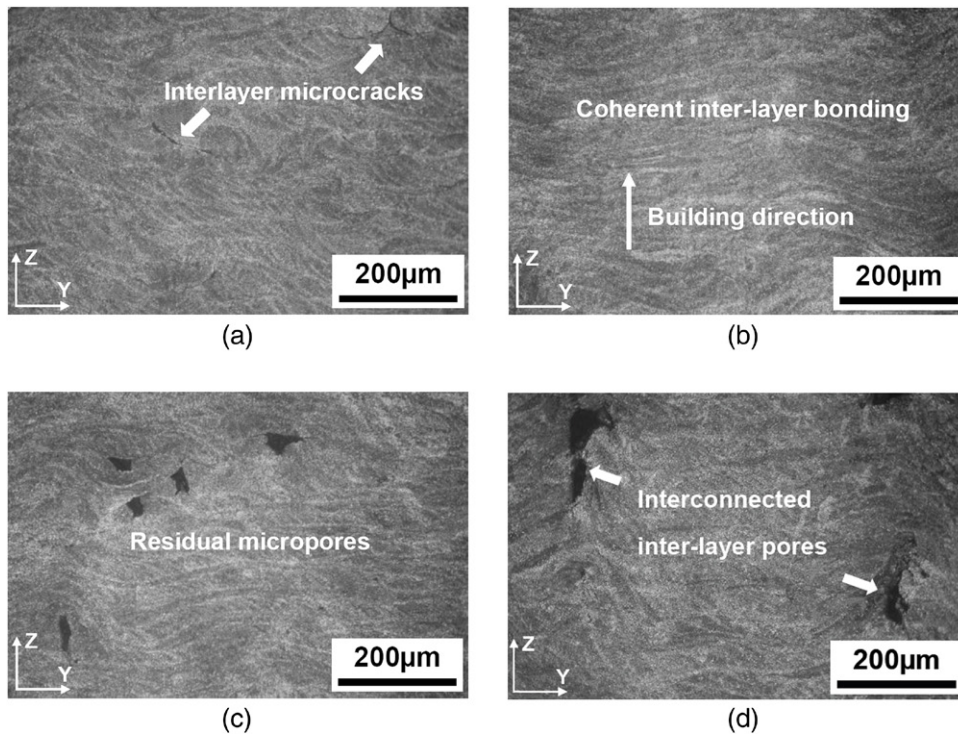

Figure 10. OM images showing interlayer microstructures on cross-sections of the SLM-processed TiC/AlSi10Mg nanocomposite parts with different laser powers while the laser scan speed is fixed as 400 mm s^{-1}: (*a*) P_1 = 200 W; (*b*) P_2 = 150 W; (*c*) P_3 = 100 W; (*d*) P_4 = 80 W.

due to the release of residual thermal stresses along the thickness direction. When the laser power decreased to 150 W, a reasonable molten pool depth of 62.8 μm was obtained, giving rise to a good interlayer bonding ability (figure 10(*b*)). On the other hand, the formation of micropores can be attributed to the balling effect, which is well known as a metallurgical defect in the SLM process. Furthermore, the underlying factor is considered to be the volume fraction of liquid AlSi10Mg phase and resultant wettability. When the applied laser power was 100 W, the calculated maximum temperature of 1390 K and liquid lifetime of 0.73 ms generated relatively poor wettability. Therefore, the limited liquid formation is insufficient to moisten surrounding powder particles, leading to large amount of residual micropores after solidification (figure 10(*c*)). As the laser power further decreased to 80 W, the lower laser energy input produced lower peak temperature of 1260 K and shorter liquid lifetime of 0.34 ms, accordingly, generating less liquid and larger micropores (figure 10(*d*)). Moreover, due to the layer-by-layer SLM process, the fluctuating surface caused by those defects is unfavourable for a uniform deposition of the fresh powder on the previously processed layer. Therefore, the interlayer pores tended to be formed at the same place and thus generated pore chains between the neighbouring layers.
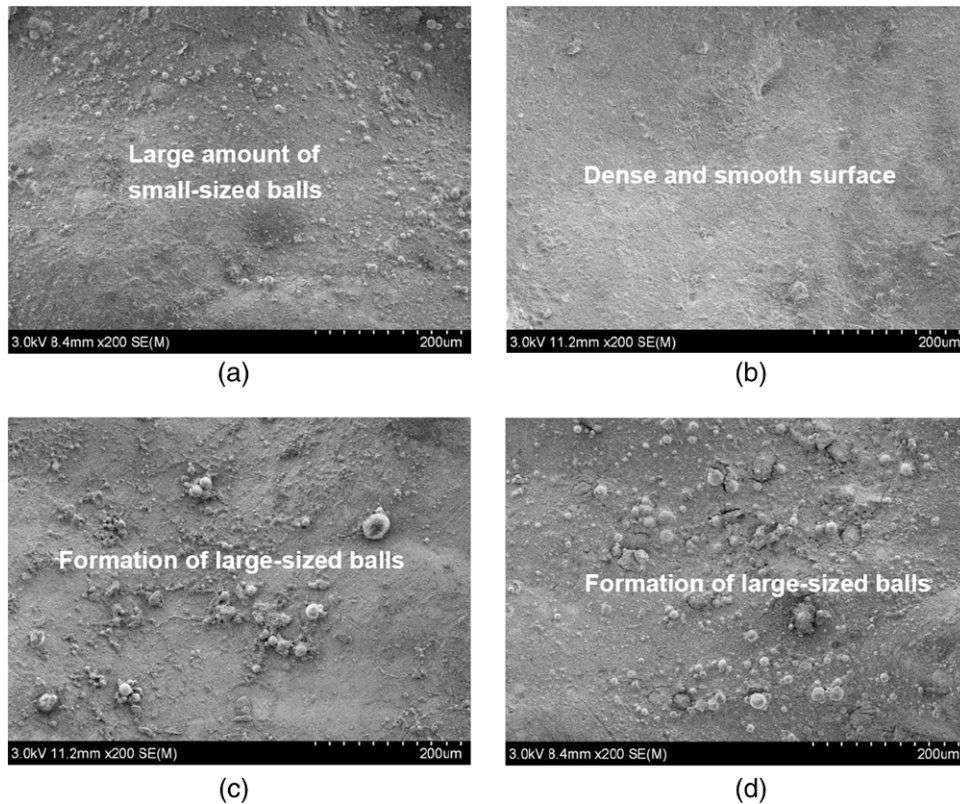
Figure 11. FE-SEM images showing typical surface morphologies of the SLM-processed TiC/AlSi10Mg parts with different laser scan speeds while the laser power is fixed as 100 W: (a) $V_1 = 100\,mm\,s^{-1}$; (b) $V_2 = 150\,mm\,s^{-1}$; (c) $V_3 = 200\,mm\,s^{-1}$; (d) $V_4 = 400\,m\,s^{-1}$.

Figure 11 depicts the typical surface morphologies of SLM-processed TiC/AlSi10Mg nanocomposite parts using various laser scan speeds and the constant laser power of 100 W. At a relatively low scan speed of 100 mm s^{-1}, a considerable rough surface consisting of a large amount of small-sized spherical balls with diameters below 10 μm were formed (figure 11(a)), implying the occurrence of balling effect at a microscopic scale. At a reasonable scan speed of 150 mm s^{-1}, a pretty dense and smooth surface was yielded, free of any balling effect and pores formation (figure 11(b)). On increasing scan speed to 200 mm s^{-1}, the metallic balls were presented on the surface again and the balls were observed larger in their sizes, with an average diameter of ~20 μm (figure 11(c)). As an even higher scan speed of 400 mm s^{-1} was applied, a great number of large-sized balls were generated on the even rougher surface. Moreover, lots of small micropores were obviously presented on the relatively loose surface, exhibiting poor densification activity.

During the SLM process, a lower scan speed of 100 mm s^{-1} leads to a longer dwelling time of the laser beam on the surface of the molten pool and attendant higher laser energy input to the pool, therefore producing higher working temperature of 1590 K. Under this condition, the dynamic viscosity of AlSi10Mg liquid within the molten pool accordingly decreases and a longer liquid lifetime of 7.41 ms is obtained, resulting in a high degree of overheating of the liquid and resultant elevated melt instability. Consequently, a large number of small-sized liquid droplets tend to splash from the surface of the molten track and then are formed into micrometre-scaled spherical balls around the solidified surface (figure 11(a)) [44]. On the other hand, the higher laser scan speed tends to produce the larger maximum temperature gradients, giving rise to higher surface tension gradients and resultant intensified Marangoni convection, hence increasing the magnitude of the thermocapillary force and attendant instability of the liquid [45–48]. Therefore, relatively coarsened balls were formed on the surface (figures 11(c) and (d)). Furthermore, when a higher scan speed of 400 mm s^{-1} was adopted, the lower operating temperature and melt viscosity were obtained, leading to the poor flowability of the liquid and resultant poor wettability. In this situation, due to the limited liquid formation, a large amount of small micropores were accordingly formed on the solidified surface (figure 11(d)).

5. Conclusions

In the present work, a three-dimensional finite volume method (FVM) model was established to investigate the temperature evolution behaviour during selective laser melting of TiC/AlSi10Mg nanocomposite. The SLM experiments were also conducted under the same laser processing parameters used in the simulation. The following conclusions can be drawn.

(a) Marangoni convection had great effects on the mass and heat transfer within the molten pool, as well as the pool geometry. With the presence of Marangoni effect, the

J. Phys. D: Appl. Phys. 48 (2015) 035303

P Yuan and D Gu

laser-induced melt pool is in a wide and shallow shape, while the molten pool turns into a narrower but deeper configuration without Marangoni effect.

(b) The simulated temperatures of the laser–powder interaction zone and the liquid lifetime increased with increasing the laser power or decreasing the laser scan speed. The maximum temperature gradient within the molten pool increased significantly with increasing the applied laser power, but increased slightly as a higher laser scan speed was adopted.

(c) The simulated molten pool length, width and depth were all found to increase with the increase of the laser power, while decreased with the increase of laser scan speed. Meanwhile, the experimentally measured three dimensions of the melt pool showed great consistence with the values predicted by simulation.

(d) When the combination of the laser processing parameters was optimized at $P = 150\,W$, $V = 400\,mm\,s^{-1}$ and $P = 100\,W$, $V = 150\,mm\,s^{-1}$, the reasonable high temperature (1560 and 1510 K) and liquid lifetime (1.41 and 4.02 ms) could be obtained, which were beneficial to acquire sound wettability and stability of the molten pool. The dense and coherent metallurgically bonded layers without any apparent pores and cracks were generated at $P = 150\,W$ and $V = 400\,mm\,s^{-1}$. Meanwhile, a pretty dense and smooth surface free of any balling effect and pores formation could be acquired when the laser process parameters were optimized at $P = 100\,W$ and $V = 150\,mm\,s^{-1}$.

(e) The transition from powder to solid, the utilization of moving laser source with a Gaussian distribution, the nonlinearities produced by temperature-dependent material properties, the convective heat transfer and fluid flow driven by surface tension were generally considered in the calculation. By exploiting these characteristics, a more accurate model could be achieved. The numerical simulation and experimental study of temperature evolution behaviour provide a good guidance for choosing the appropriate processing parameters to yield a feasible operating temperature during SLM.

Acknowledgments

References

[1] Prasad S V and Asthana R 2004 *Tribol. Lett.* **17** 445–53
[2] Kumar S S, Bai V S, Rajkumar K V, Sharma G K, Jayakumar T and Rajasekharan T 2009 *J. Phys. D: Appl. Phys.* **42** 175504
[3] Kumar S S, Bai V S and Rajasekharan T 2008 *J. Phys. D: Appl. Phys.* **41** 105403
[4] Yi H Z, Ma N H, Zhang Y J, Li X F and Wang H W 2006 *Scr. Mater.* **54** 1093–7
[5] Fogagnolo J B, Velasco F, Robert M H and Torralba J M 2003 *Mater. Sci. Eng.* A **342** 131–43
[6] Hesabi Z R, Simchi A and Reihani S M 2006 *Mater. Sci. Eng.* A **428** 159–68
[7] Simchi A and Godlinski D 2011 *J. Mater. Sci.* **46** 1446–54
[8] Kennedy A R and Wyatt S M 2001 *Composites* A **32** 555–9
[9] Tong X C and Ghosh A K 2001 *J. Mater. Sci.* **36** 4059–69
[10] Gu D D, Meiners W, Wissenbach K and Poprawe R 2012 *Int. Mater. Rev.* **57** 133–64
[11] Gu D D, Meiners W, Hagedorn Y C, Wissenbach K and Poprawe R 2010 *J. Phys. D: Appl. Phys.* **43** 295402
[12] Yadroitsev I, Bertrand P and Smurov I 2007 *Appl. Surf. Sci.* **253** 8064–9
[13] Xiao B and Zhang Y W 2007 *J. Phys. D: Appl. Phys.* **40** 6725–34
[14] Körner C, Bauereiß A and Attar E 2013 *Modell. Simul. Mater. Sci. Eng.* **21** 085011
[15] Louvis E, Fox P and Sutcliffe C J 2011 *J. Mater. Process. Technol.* **211** 275–84
[16] Brandl E, Heckenberger U, Holzinger V and Buchbinder D 2012 *Mater. Des.* **34** 159–69
[17] Buchbinder D, Schleifenbaum H, Heidrich S, Meiners W and Bültmann J 2011 *Phys. Procedia* **12** 271–8
[18] Thijs L, Kempen K, Kruth J P and Humbeeck J V 2013 *Acta Mater.* **61** 1809–19
[19] Pinkerton A J and Li L 2004 *J. Phys. D: Appl. Phys.* **37** 1885–95
[20] Safdar S, Li L and Sheikh M A 2007 *J. Phys. D: Appl. Phys.* **40** 593–603
[21] He X, Yu G and Mazumder J 2010 *J. Phys. D: Appl. Phys.* **43** 015502
[22] Roberts I A, Wang C J, Esterlein R, Stanford M and Mynors D J 2009 *Int. J. Mach. Tools Manuf.* **49** 916–23
[23] Yadroitsev I, Gusarov A, Yadroitsava I and Smurov I 2010 *J. Mater. Process. Technol.* **210** 1624–31
[24] Zhang D Q, Cai Q Z, Liu J H, Zhang L and Li R D 2010 *Int. J. Adv. Manuf. Technol.* **51** 649–58
[25] Chan C, Mazumder J and Chen M M 1984 *Metall. Trans.* A **15** 2175–84
[26] Qi H and Mazumder J 2006 *J. Appl. Phys.* **100** 024903
[27] He X L, Song L J, Yu G and Mazumder J 2011 *Appl. Surf. Sci.* **258** 898–907
[28] Dou L, Yuan Z F, Li J Q, Li J and Wang X Q 2008 *Chin. Sci. Bull.* **53** 2593–8
[29] Wang H, Shi Y W and Gong S L 2006 *J. Phys. D: Appl. Phys.* **39** 4722–30
[30] Labudovic M, Hu D and Kovacevic R 2003 *J. Mater. Sci.* **38** 35–49
[31] Kruth J P, Wang X, Laoui T and Froyen L 2003 *Assembly Autom.* **23** 357–71
[32] Dai K and Shaw L 2005 *Acta Mater.* **53** 4743–54
[33] Yang J and Wang F 2009 *Int. J. Adv. Manuf. Technol.* **43** 1060–8
[34] Pang S Y, Chen L L, Zhou J X, Yin Y J and Chen T 2011 *J. Phys. D: Appl. Phys.* **44** 025301
[35] Cui H C, Lu F G, Tang X H and Yao S 2012 *Acta Metall. Sin.* **25** 190–200
[36] Vasantgadkar N A, Bhandarkar U V and Joshi S S 2010 *Thin Solid Films* **519** 1421–30
[37] Kruth J P, Mercelis P, Vaerenbergh J V, Froyen L and Rombouts M 2005 *Rapid Prototyping J.* **11** 26–36

J. Phys. D: Appl. Phys. **48** (2015) 035303

P Yuan and D Gu

[38] Rombouts M, Froyen L, Gusarov A V, Bentefour E H and Glorieux C 2005 *J. Appl. Phys.* **98** 013533

[39] Yin H B and Emi T 2003 *Metall. Mater. Trans.* B **34** 483–93

[40] Xu Y L, Dong Z B, Wei Y H and Yang C L 2007 *Theor. Appl. Fract. Mech.* **48** 178–86

[41] Yin J, Zhu H H, Ke L, Lei W J, Dai C and Zuo D L 2012 *Comput. Mater. Sci.* **53** 333–9

[42] Simchi A 2006 *Mater. Sci. Eng.* A **428** 148–58

[43] Gu D D and Shen Y F 2007 *J. Alloys Compounds* **432** 163–6

[44] Gu D D and Shen Y F 2009 *Mater. Des.* **30** 2903–10

[45] Zhang B C, Dembinski L and Coddet C 2013 *Mater. Sci. Eng.* A **584** 21–31

[46] Li R D, Shi Y S, Wang Z G, Wang L, Liu J H and Jiang W 2010 *Appl. Surf. Sci.* **256** 4350–56

[47] Zhang B C, Liao H L and Coddet C 2012 *Mater. Des.* **34** 753–8

[48] Zhang B C, Liao H L and Coddet C 2013 *Vacuum* **95** 25–9